MCD18 V6.2: A New Version of MODIS Downward Shortwave Radiation and Photosynthetically Active Radiation Products

Ruohan Li, Dongdong Wang, *Senior Member, IEEE*, Sadashiva Devadiga, *Member, IEEE*, Sudipta Sarkar, and Miguel O. Román

***Abstract*— This study presents the new version of MODIS/Terra + Aqua Surface Radiation Daily/3-h downward shortwave radiation (DSR) (MCD18A1 V6.2) and photosynthetic active radiation (PAR) (MCD18A2 V6.2) product generated by MODIS adaptive processing system (MODAPS) using the latest version of the science algorithm developed by the NASA MODIS land science team. Key improvements in the new algorithm include using multiple bands covering visible, near-infrared, and shortwave infrared to enhance the capability of characterizing cloud optical characteristics, especially over snow-covered surfaces, and adopting linear interpolation for temporal scaling from instantaneous to 3-hourly retrievals. Comparative validation against MCD18 V6.1 and clouds and the Earth's radiant energy system synoptic (CERES-SYN) demonstrates that V6.2 significantly improves accuracy at instantaneous, 3-hourly, and daily scales, particularly in snow-covered regions. The root mean square error (RMSE) (relative RMSE: rRMSE) of V6.2 reaches 101.9 W/m^2 (18.8%) and 48.4 W/m^2 (20.8%) for instantaneous DSR and PAR. The RMSE (rRMSE) reaches 29.9 W/m^2 (16.9%) and 14.1 W/m^2 (18.4%) for daily DSR and PAR, respectively. Aggregated to 100 km, V6.2 matches CERES-SYN accuracy using only polar-orbiting satellite data. This study also explores the potential for future improvement by integrating geostationary observations to enhance accuracy further.**

***Index Terms*— Downward shortwave radiation (DSR), look-up table (LUT), photosynthetic active radiation (PAR), remote sensing, satellite products.**

I. Introduction

SOLAR radiation is a fundamental energy source for the Earth, driving various natural processes essential for life and the environment [1]. Downward shortwave radiation (DSR), with wavelengths ranging from 300 to 4000 nm, fuels global ecological, hydrological, biophysical, and biochemical processes. It plays a crucial role in weather and climate change predictions [2], [3]. Additionally, it is an important renewable energy source for photovoltaic (PV) power generation [4]. Within this spectrum, photosynthetically active radiation (PAR), spanning 400–700 nm, is vital for photosynthesis, making it essential for terrestrial ecosystem modeling, carbon cycle modeling, and agricultural growth modeling [5].

Several global satellite products of surface radiative fluxes have been produced. Many widely used products have a coarse spatial resolution and have not been updated since the 2000s, such as the International Satellite Cloud Climatology Project (ISCCP) product on a 280-km equal-area global grid from 1983 to 2008 [6], the global energy and water cycle experiment (GEWEX) surface radiation budget (SRB) product at a spatial resolution of 1° × 1° (∼110 km) from 1983 to 2007 [7]. The clouds and the Earth's radiant energy system (CERES) are still in production but at a spatial resolution of 1° [8]. In recent years, high-resolution radiation products have been generated. The European Organization for the Exploitation of Meteorological Satellites (EUMETSAT) published the CLARA-A3 radiation product at 0.25° (∼25 km) resolution. Still, it only includes the DSR variables and the snow-covered regions are excluded [9]. Other products, including DSCOVR/EPIC hourly DSR/PAR at 0.1° (∼10 km) resolution [10] and breathing Earth system simulator (BESS) at 5 km every four days resolution [11], are based on data-driven methods.

MCD18 V6.1 (V6.1), a product generated by NASA's MODIS land science team, is the first version of the operational MODIS global daily DSR product [12]. It is based on the combined MODIS Terra and Aqua observations and applied the look-up table (LUT) approach originally proposed by [13]. The reliability of the approach and data has been fully validated [12], [14]. Since its publication in 2017, it has been used as the input source for many other high-resolution datasets, including land surface temperature [15], land surface albedo [16], evapotranspiration [17], surface ozone [18], and so on. It also has been extensively used to address global and regional scientific issues, including vegetation net primary productivity response to COVID-19 lockdown [19] and ecosystem water use efficiency response to drought [20].

Received 11 September 2024; revised 30 October 2024 and 17 November 2024; accepted 20 November 2024. Date of current version 5 December 2024. This work was supported by NASA under Grant 80NSSC21K0701. *(Corresponding author: Dongdong Wang.)*

Ruohan Li and Dongdong Wang are with the Department of Geographical Sciences, University of Maryland, College Park, MD 20742, USA (e-mail: r526li@umd.edu; ddwang@umd.edu).

Sadashiva Devadiga and Sudipta Sarkar are with the Terrestrial Information Systems Laboratory, NASA Goddard Space Flight Center, Greenbelt, MD 20771, USA (e-mail: sadashiva.devadiga-1@nasa.gov; sudipta.sarkar@nasa.gov).

Miguel O. Román is with the Earth Sciences Division, NASA Goddard Space Flight Center, Greenbelt, MD 20771, USA (e-mail: miguel.o.roman@nasa.gov).

Digital Object Identifier 10.1109/LGRS.2024.3507822

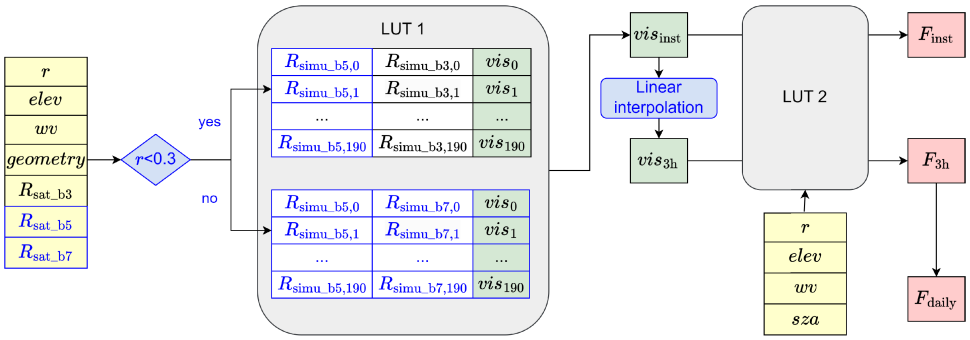

Fig. 1. Algorithm description of MCD18 V6.2.

However, V6.1 exhibits degradation in high-latitude regions, particularly over snow-covered and cloudy pixels [21]. This is mainly due to the use of a single blue band in the original algorithms, which easily saturates over highly reflective cases like snow and clouds. Consequently, it becomes challenging to distinguish between surface and atmospheric reflections, leading to significant biased estimation of radiation over snow-covered areas. Additionally, systematic bias is observed in the 3-hourly validations, stemming from the nearest-neighbor interpolation methods used with the limited daily MODIS overpasses.

MCD18 V6.2 (V6.2) is derived from the same V6.1 branch, addressing the previously identified issues by enhancing the single-band LUT method used in V6.1. The updates include the implementation of a multiband LUT algorithm and linear temporal interpolation, which improve the retrieval accuracy. Section II describes the revised method, validation data, and validation metrics. Section III presents the validation results of the new version. Section IV discusses the future directions of the data, and Section V summarizes the study.

II. Methods and Data

A. Algorithm Description

The algorithm of this new version is revised from the LUT approach adopted in the previous version (Fig. 1). The original LUT approach uses two LUTs generated from the numerical atmospheric radiative transfer models. The theoretical background of the method can be found in [12]. LUT one aims to retrieve the atmospheric conditions by comparing the satellite-observed top of atmosphere (TOA) reflectance R_{sat} and the simulated TOA reflectance R_{simu} based on surface reflectance (r), total precipitable water vapor (wv), elevation (elev), geometry including solar zenith angle (sza), viewing zenith angle (vza), and relative azimuth angle (raa). The atmospheric condition is represented by the visibility index vis. The retrieved vis from LUT one combined with additional inputs including r, wv, elev, and sza are used for LUT two to determine the surface flux F. For DSR and PAR, the workflows are the same but separate tables are generated.

The main improvements in the current version are highlighted in blue in Fig. 1. First, the original method used only the blue band of MODIS (band 3) to retrieve the atmospheric conditions. However, the blue band will easily be saturated over highly reflective regions [21]. Hence, it is prone to degradation over cloudy and snow-cloud-mixed pixels. This method includes additional near-infrared bands (band 5) and shortwave infrared bands (band 7) to address this issue. The dual-band method for cloud properties retrieval is adopted, inspired by the study [22]. When r is lower than 0.3, bands 3 and 5 are used; otherwise, bands 5 and 7 are used. The threshold of 0.3 was chosen because it effectively distinguishes between nonsnow and snow-covered cases across various scenarios. The vis_k is selected where the sum of the differences between $R_{\text{sat\_}bi,k}$ and $R_{\text{simu\_}bi,k}$, and $R_{\text{sat\_}bj,k}$ and $R_{\text{simu\_}bj,k}$ are the smallest:

$$\text{vis}_k = \arg\min_k \left(|R_{\text{sat\_}bi,k} - R_{\text{simu\_}bi,k}| + |R_{\text{sat\_}bj,k} - R_{\text{simu\_}bj,k}| \right). \quad (1)$$

Previous methods used the nearest neighborhood to interpolate the instantaneous visibility index (vis_{inst} to the 3-h visibility index (vis_{3h}). In this new version, the visibility index at time $t2$ is linearly interpolated from visibility at time $t1$ and $t3$ as the following equation:

$$\text{vis}_{t2} = \text{vis}_{t1} * (t2 - t1)/(t3 - t1) + \text{vis}_{t3} * (t3 - t2)/(t3 - t1). \quad (2)$$

After receiving vis_{inst} and vis_{3h}, the corresponding fluxes F_{inst} and F_{3h} are calculated separately using the LUT two. The daily fluxes F_{daily} take the average of F_{3h}.

The input variables and data source remain the same as the previous version, which is listed in Table I. All data are gridded into the MODIS sinusoidal map projection before feeding into the algorithm.

TABLE I
Input Data Sources and Their Spatial and Temporal Resolution

Input Variable	Source	S. Resolution	T. Resolution
TOA reflectance	MODIS	1km	Instantaneous
Geometry	MODIS	1km	Instantaneous
Surface albedo	MCD43A3	500m	Daily
	Climatology	1km	Daily
Precipitable water vapor	MERRA2	$0.5 \times 0.625°$	Hourly
Surface elevation	GTOPO30	30 arcsec	Static

B. Validation Data

Given that V6.1 has already undergone comprehensive global validation, this study includes data from seven surface radiation budget network (SURFRAD) sites [23] to demonstrate the improvements in V6.2 by comparison with V6.1. Additionally, four Greenland climate network (GC-NET) [24]

TABLE II
SUMMARY OF GROUND MEASUREMENT SITES

Name	Network	Latitude (°)	Longitude (°)	Elevation (m)
BND	SURFRAD	40.05	-88.37	230
FPK	SURFRAD	48.31	-105.10	634
GWN	SURFRAD	34.25	-89.87	98
DRA	SURFRAD	36.62	-116.02	1007
PSU	SURFRAD	40.72	-77.93	376
SXF	SURFRAD	43.73	-96.62	473
TBL	SURFRAD	40.12	-105.24	1689
NAU	GCNET	73.84	-49.50	2333
SUM	GCNET	72.58	-38.50	3204
DY2	GCNET	66.48	-46.28	2111
HUM	GCNET	78.53	-56.83	1955

sites were chosen due to known issues in snow-covered areas in previous versions, allowing us to assess the improvements in V6.2. The specific locations of each site are detailed in Table II. SURFRAD provides high-quality measurements of DSR and PAR on a minute-by-minute basis. This comprehensive measurement of these radiation components enables a thorough evaluation of V6.2 across various time scales. GC-NET measures DSR hourly across Greenland regions, which helps verify improvements in snow-covered areas. Data from both SURFRAD and GC-NET have undergone rigorous quality checks. Additionally, the data are preprocessed, cleaned, and aggregated following the method described in [21].

In addition to comparing V6.1 and V6.2, we also compared them with clouds and the Earth's radiant energy system synoptic (CERES-SYN) data which covers globally with a 1° spatial resolution. It retrieves DSR from multiple sources including polar orbiting CERES, MODIS, geostationary satellite observations, reanalysis data from the GEOS, and other sources [8], [25]. The data have shown the highest accuracy among the global DSR products [21] and are hence used as the baseline results in many studies [26]. We will continue to explore new products as they emerge to further enhance comparisons and ensure rigorous validation of the MCD18 dataset.

C. Validation Metrics

In this study, we applied metrics R^2, mean bias difference (MBD), and root mean square error (RMSE) to validate the satellite retrieved radiation F_s with ground-measured radiation F_g. The relative RMSE (rRMSE) is also included to enable a more fair comparison at different local times, regions, and with other studies. The metrics are calculated as the following equations:

$$\mathrm{MBD} = \frac{1}{N}\sum_{i=1}^{N}\left(F_s^i - F_g^i\right) \tag{3}$$

$$\mathrm{RMSE} = \sqrt{\frac{1}{N}\sum_{i=1}^{N}\left(F_s^i - F_g^i\right)^2} \tag{4}$$

$$\mathrm{rRMSE} = \frac{\mathrm{RMSE}}{\overline{F_g}}. \tag{5}$$

III. VALIDATION RESULTS

In this section, we comprehensively validate V6.2 and compare it with V6.1 and CERES-SYN to demonstrate its enhanced accuracy. We assess these datasets across different temporal scales and over Greenland regions, highlighting the effectiveness of the new algorithms that utilize multiband data and linear interpolation methods.

TABLE III
SUMMARY OF THE VALIDATION RESULTS OF INSTANTANEOUS AND DAILY DSR AND PAR AT EACH SURFRAD SITE

	DSR				PAR			
	R^2	MBD (W/m^2)	RMSE (W/m^2)	rRMSE (%)	R^2	MBD (W/m^2)	RMSE (W/m^2)	rRMSE (%)
Instantaneous								
V6.1	0.866	-20.7	118.3	21.9	0.846	-0.6	55.8	24.0
V6.2	0.884	-0.6	101.9	18.8	0.871	8.4	48.4	20.8
Daily								
V6.1	0.896	-6.0	37.5	21.1	0.894	-0.6	16.9	22.1
V6.2	0.922	-1.9	29.9	16.9	0.918	1.3	14.1	18.4

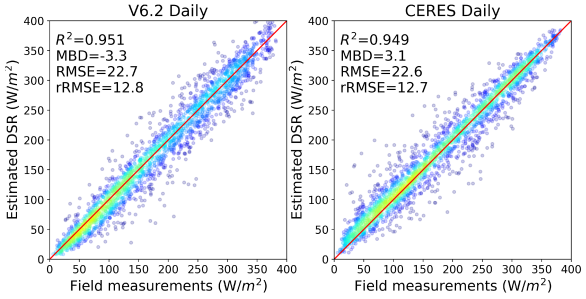

Fig. 2. Comparison of V6.2 daily DSR over SURFRAD sites with CERES-SYN after aggregating into 100 km.

A. Overall Validation

The validation results of instantaneous and daily estimation of DSR and PAR over SURFRAD sites are listed in Table III. It is pronounced that V6.2 has a better performance of all variables at both instantaneous and daily scales. For instantaneous DSR, the RMSE improves from 118.3 to 101.9 W/m^2 and the RMSE improves from 55.8 to 48.4 W/m^2 for instantaneous PAR estimation. At the daily scale, the RMSE of estimating DSR improves from 37.5 to 29.9 W/m^2, and of estimating PAR improves from 16.9 to 14.1 W/m^2. The rRMSE of both DSR and PAR at different scales are all within 20%.

To further demonstrate the high accuracy of the new version, we compared the daily DSR retrieval with CERES over SURFRAD sites as shown in Fig. 2. Since CERES has a resolution of 1°, we aggregate V6.2 to 100 km for a fair comparison. V6.2 and CERES present very similar results in all metrics. The R^2 are 0.951 and 0.949, the MBD are −3.3 and 3.1 W/m^2, and the RMSE are 22.7 and 22.6 W/m^2 for V6.2 and CERES, respectively. It is noteworthy that CERES-SYN used both polar-orbiting satellite data, such as MODIS and CERES, and geostationary satellite observations for temporal interpolation. It is promising that V6.2, which utilizes only MODIS observations, achieves accuracy comparable to that of CERES-SYN.

B. Validation at 3-Hourly Scales

The new temporal interpolation methods have significantly improved MCD18 performance at 3-hourly and daily scales.

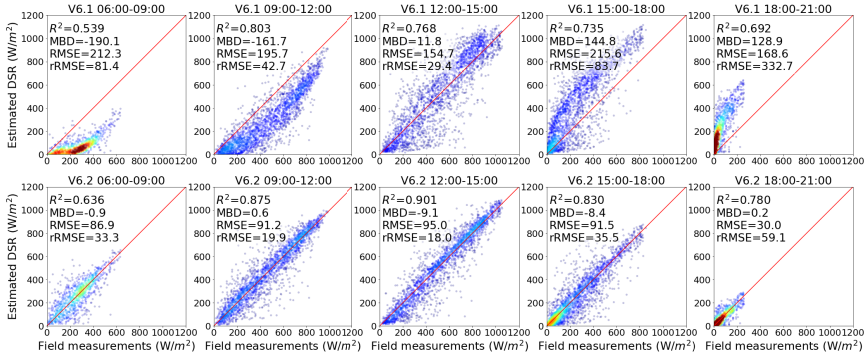

Fig. 3. Validation results of V6.1 and V6.2 3-h DSR in local time over SURFRAD sites.

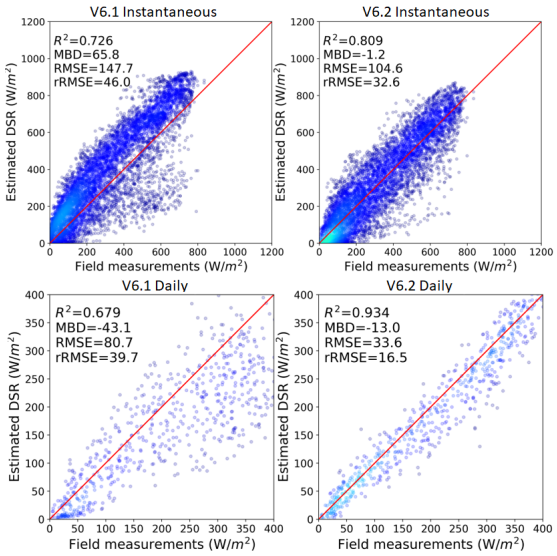

Fig. 4. Validation results of V6.1 and V6.2 instantaneous and daily DSR over GCNET.

Fig. 3 shows validation results over SURFRAD sites at a 3-hourly scale. For both versions, the best performance is observed at UTC 18, with accuracy decreasing as time moves away from this point. This is partly because UTC 18 corresponds to a smaller solar zenith angle, contributing to more accurate estimations, and more likely, it is closest to the MODIS overpass time at 1 PM local time. Temporal interpolation introduces increasing uncertainties over time. The new version shows less skewing across all UTC times. The absolute MBD exceeded 100 W/m^2 in the old version, except at overpass time, while V6.2 remains within 10 W/m^2 for all times. Although the trend of lowest rRMSE at overpass time persists in the new version, its magnitude is much lower, with rRMSE within 60%. These results demonstrate the effectiveness of the linear interpolation method applied in V6.2.

C. Validation Over Greenland

We also evaluated the estimated DSR over Greenland to show the improvement of the new multiband algorithm over snow-covered cases. The validation results of both daily and instantaneous DSR are shown in Fig. 4. For instantaneous estimation, the RMSE (rRMSE) improves from 147.7 W/m^2 (46%) to 104.6 W/m^2 (32.6%). The MBD was previously 65.8 W/m^2, largely due to the inability to distinguish between cloud and snow, and has been improved to -1.2 W/m^2. At a daily scale, the RMSE (rRMSE) improves from 80.7 W/m^2 (39.7%) to 33.6 W/m^2 (16.5%). The MBD also largely improves from -43.1 to -13.0 W/m^2. It is noticeable that the magnitude of improvement for both daily and instantaneously estimation over GCNET is larger than it is over SURFRAD stations, demonstrating the superior performance of the new algorithm over snow-covered regions.

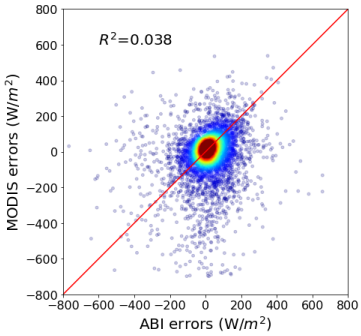

Fig. 5. Correlation between ABI and MODIS retrieved errors.

IV. Discussion

Although MCD18 V6.2 has shown high accuracy with high spatial and temporal resolutions, further improvements can be achieved by incorporating geostationary sensors such as the advanced Himawari imager (AHI) and advanced baseline imager (ABI). As introduced in [21], the LUT has been applied to both MODIS and ABI observations and combined estimations from both sensors using the optimization approach proposed in [27]. The combined results show higher accuracy compared to applying the method individually to each sensor [21]. This enhancement is due to the low correlation between ABI and MODIS retrieved errors (R^2 = 0.038) as shown in Fig. 5, which arises from differences in radiometric calibration, geometric registration, spectral configuration, view geometry, and ground footprint for the two types of sensors. By integrating retrievals from both sensors, future improvements can leverage the high temporal resolution of geostationary sensors and the global coverage of MODIS, effectively enhancing accuracy in overlapping

areas and providing comprehensive global coverage with high temporal resolution.

V. Conclusion

This study introduces the new version of MODIS/Terra + Aqua Surface Radiation Daily/3-h DSR/PAR data (MCD18 V6.2). The original algorithm is refined mainly in two ways: first, by using multiple bands, including both visible, NIR, and SWIR, rather than the single blue band in the existing LUT approach to better distinguish cloud from snow; second, by replacing the nearest neighbor method with linear interpolation for temporal interpolation from instantaneous retrieval to 3-hourly retrieval. We validated and compared the V6.2 with V6.1 and CERES-SYN data. The overall validation results at instantaneous and daily scales are significantly better than V6.1 for both DSR and PAR. After aggregating into 100 km, the accuracy of MCD18 V6.2 is comparable to CERES-SYN but with only polar-orbiting satellite observations as input. Additionally, V6.2 shows notable improvements at the 3-h scale and over snow-covered regions. Future directions will incorporate geostationary observations to further improve MCD18's accuracy.

References

[1] S. Liang, D. Wang, T. He, and Y. Yu, "Remote sensing of Earth's energy budget: Synthesis and review," *Int. J. Digit. Earth*, vol. 12, no. 7, pp. 737–780, Mar. 2019.

[2] G. Huang et al., "Estimating surface solar irradiance from satellites: Past, present, and future perspectives," *Remote Sens. Environ.*, vol. 233, Nov. 2019, Art. no. 111371.

[3] P. J. Sellers et al., "Modeling the exchanges of energy, water, and carbon between continents and the atmosphere," *Science*, vol. 275, no. 5299, pp. 502–509, 1997.

[4] R. Li, D. Wang, W. Wang, and R. Nemani, "A GeoNEX-based high-spatiotemporal-resolution product of land surface downward shortwave radiation and photosynthetically active radiation," *Earth Syst. Sci. Data*, vol. 15, no. 3, pp. 1419–1436, Mar. 2023.

[5] X. Xiao et al., "Satellite-based modeling of gross primary production in a seasonally moist tropical evergreen forest," *Remote Sens. Environ.*, vol. 94, no. 1, pp. 105–122, Jan. 2005.

[6] Y. Zhang, W. B. Rossow, A. A. Lacis, V. Oinas, and M. I. Mishchenko, "Calculation of radiative fluxes from the surface to top of atmosphere based on ISCCP and other global data sets: Refinements of the radiative transfer model and the input data," *J. Geophys. Res., Atmos.*, vol. 109, no. 19, Oct. 2004, Art. no. D19105.

[7] R. T. Pinker and I. Laszlo, "Modeling surface solar irradiance for satellite applications on a global scale," *J. Appl. Meteorol.*, vol. 31, no. 2, pp. 194–211, Feb. 1992.

[8] D. A. Rutan et al., "CERES synoptic product: Methodology and validation of surface radiant flux," *J. Atmos. Ocean. Technol.*, vol. 32, no. 6, pp. 1121–1143, Jun. 2015.

[9] K.-G. Karlsson et al., "CLARA-a3: The third edition of the AVHRR-based CM SAF climate data record on clouds, radiation and surface albedo covering the period 1979 to 2023," *Earth Syst. Sci. Data*, vol. 15, no. 11, pp. 4901–4926, Nov. 2023.

[10] D. Hao et al., "DSCOVR/EPIC-derived global hourly and daily downward shortwave and photosynthetically active radiation data at $0.1^\circ \times 0.1^\circ$ resolution," *Earth Syst. Sci. Data*, vol. 12, no. 3, pp. 2209–2221, 2020.

[11] Y. Ryu, C. Jiang, H. Kobayashi, and M. Detto, "MODIS-derived global land products of shortwave radiation and diffuse and total photosynthetically active radiation at 5 km resolution from 2000," *Remote Sens. Environ.*, vol. 204, pp. 812–825, Jan. 2018.

[12] D. Wang, S. Liang, Y. Zhang, X. Gao, M. G. L. Brown, and A. Jia, "A new set of MODIS land products (MCD18): Downward shortwave radiation and photosynthetically active radiation," *Remote Sens.*, vol. 12, no. 1, p. 168, Jan. 2020.

[13] S. Liang, T. Zheng, R. Liu, H. Fang, S. Tsay, and S. Running, "Estimation of incident photosynthetically active radiation from moderate resolution imaging spectrometer data," *J. Geophys. Res., Atmos.*, vol. 111, no. 15, Aug. 2006, Art. no. D15208.

[14] D. Wang, S. Liang, R. Li, and A. Jia, "A synergic study on estimating surface downward shortwave radiation from satellite data," *Remote Sens. Environ.*, vol. 264, Oct. 2021, Art. no. 112639.

[15] A. Jia, H. Ma, S. Liang, and D. Wang, "Cloudy-sky Land Surface Temperature from VIIRS and MODIS satellite data using a surface energy balance-based method," *Remote Sens. Environ.*, vol. 263, Sep. 2021, Art. no. 112566.

[16] A. Jia, D. Wang, S. Liang, J. Peng, and Y. Yu, "Global daily actual and snow-free blue-sky land surface albedo climatology from 20-year MODIS products," *J. Geophys. Res., Atmos.*, vol. 127, no. 8, Apr. 2022, Art. no. e2021JD035987.

[17] T. Rashid and D. Tian, "Improved 30-m evapotranspiration estimates over 145 eddy covariance sites in the contiguous United States: The role of ECOSTRESS, harmonized Landsat Sentinel-2 imagery, climate reanalysis, and deep neural network postprocessing," *Water Resour. Res.*, vol. 60, no. 4, Apr. 2024, Art. no. e2021JD035987.

[18] F. Cheng et al., "First retrieval of 24-hourly 1-km-resolution gapless surface ozone (O3) from space in China using artificial intelligence: Diurnal variations and implications for air quality and phytotoxicity," *Remote Sens. Environ.*, vol. 316, Jan. 2025, Art. no. 114482.

[19] Y. Li, S. Huang, P. Fang, Y. Liang, J. Wang, and N. Xiong, "Vegetation net primary productivity in urban areas of China responded positively to the COVID-19 lockdown in spring 2020," *Sci. Total Environ.*, vol. 916, Mar. 2024, Art. no. 169998.

[20] X. Luo, Y. Wang, and Y. Li, "Responses of ecosystem water use efficiency to drought in the Lancang–Mekong river basin," *Frontiers Ecology Evol.*, vol. 11, May 2023, Art. no. 1203725.

[21] R. Li, D. Wang, and S. Liang, "Comprehensive assessment of five global daily downward shortwave radiation satellite products," *Sci. Remote Sens.*, vol. 4, Dec. 2021, Art. no. 100028.

[22] T. Nakajima and M. D. King, "Determination of the optical thickness and effective particle radius of clouds from reflected solar radiation measurements. Part I: Theory," *J. Atmos. Sci.*, vol. 47, pp. 1878–1893, Aug. 1990.

[23] J. A. Augustine, J. J. DeLuisi, and C. N. Long, "SURFRAD—A national surface radiation budget network for atmospheric research," *Bull. Amer. Meteorological Soc.*, vol. 81, no. 10, pp. 2341–2358, 2000.

[24] D. Houtz et al. (2020). *Greenland Climate Network (GC-Net) Data*. [Online]. Available: https://www.envidat.ch/dataset/gcnet

[25] D. R. Doelling et al., "Geostationary enhanced temporal interpolation for CERES flux products," *J. Atmos. Ocean. Technol.*, vol. 30, no. 6, pp. 1072–1090, Jun. 2013.

[26] R. Li, D. Wang, S. Liang, A. Jia, and Z. Wang, "Estimating global downward shortwave radiation from VIIRS data using a transfer-learning neural network," *Remote Sens. Environ.*, vol. 274, Jun. 2022, Art. no. 112999.

[27] D. Wang and S. Liang, "Improving LAI mapping by integrating MODIS and CYCLOPES LAI products using optimal interpolation," *IEEE J. Sel. Topics Appl. Earth Observ. Remote Sens.*, vol. 7, no. 2, pp. 445–457, Feb. 2014.